JACS
JOURNAL OF THE AMERICAN CHEMICAL SOCIETY
pubs.acs.org/JACS
Article

3D-Printed Porous Supramolecular Sorbents for Cobalt Recycling

Keldy S. Mason,[†] Sheng-Yin Huang,[†] Samuel K. Emslie, Qian Zhang, Simon M. Humphrey, Jonathan L. Sessler,* and Zachariah A. Page*

Cite This: J. Am. Chem. Soc. 2024, 146, 4078−4086
Read Online
ACCESS | Metrics & More | Article Recommendations | Supporting Information

ABSTRACT: Electronic waste recycling is a recognized global challenge that requires new strategies to bind and release critical materials selectively, such as cobalt present in lithium-ion batteries. To address this challenge, hierarchical 3D-printed porous polymer scaffolds bearing supramolecular receptors were prepared using vat photopolymerization and their cobalt binding profiles were examined as a function of matrix polarity. By combining high-resolution digital light processing (DLP) with polymerization-induced phase separation (PIPS), functional acrylic copolymer networks with micrometer-level precision of geometry and nanometer-level pores were generated. Covalent integration of a methacrylate-functionalized bisdicyclohexyl acetamide (BDCA-MA) receptor enabled binding and release of cobalt(II) chloride ($CoCl_2$) via a solvent polarity switch mechanism involving a change in solvent from ethanol to water. The present structures proved reusable as shown by sustained high binding efficiency over five bind and release cycles. This platform represents a "green" and energy conscious method for future electronic waste recycling.

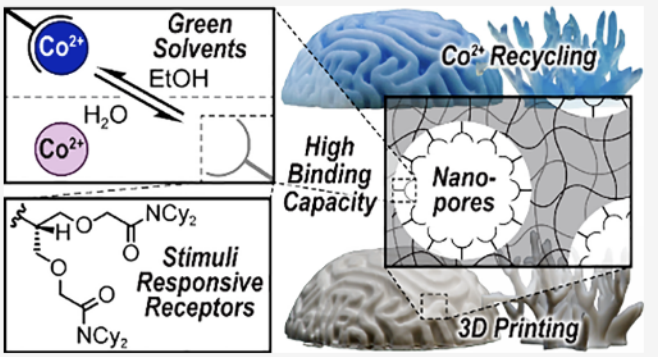

INTRODUCTION

Cobalt is an essential element required for a range of technologies such as (e.g., electric vehicles).[1−3] It is also a critical material that suffers from international supply chain instability. Exacerbating the availability problem is that over 70% of cobalt production occurs in the Democratic Republic of Congo (DRC), where mining and refinement practices are detrimental to both human health and the environment.[3,4] Recycling cobalt from end-of-life waste offers a possible self-sufficient and sustainable solution to these issues (Figure 1A).[5,6] Conventional metallurgical recycling approaches rely primarily on liquid−liquid extraction (LLE) using phosphorus-containing ligands, such as Cyanex 272.[7,8] Although effective, third phase formation (i.e., emulsion), secondary waste generation, and loss of extractant limits the widespread use of LLE for cobalt recycling (Figure 1B).[9] Thus, alternatives to LLE that require fewer processing steps, minimize waste, and enhance extractant reuse are needed.

Immobilized receptors combine ease of reuse with tunable selectivity and affinity, making them an attractive platform for critical material recycling.[10] Furthermore, noncovalent (e.g., ionic) interactions with supramolecular receptors are highly dependent on environmental factors, such as solvent polarity, which enables on-demand bind-and-release. Recently, such an approach has been investigated by our group for selective recovery of lithium from LiCl[11] and $LiPF_6$,[12] using acetonitrile-to-methanol solvent switching to promote uptake and release (Figure 1B). In these strategies, we synthesized receptor-laden organo-gels[11] and polystyrene beads[12] via direct copolymerization and post-functionalization, respectively. However, these fabrication methods have geometric design constraints, and the resultant materials are either mechanically weak or have low surface area-to-volume ratios and thus poor ion capacity densities. As an alternative, nanoporous inclusions in granular separation systems (i.e., beads) have been used to maximize the surface area-to-volume ratio for capturing a wide range of analytes such as Li,[13] Na, Ca,[14] Co, Ni,[15] Mo, V,[16] and Eu.[17] However, their operation is energy intensive owing to the high pressures required for sufficient fluid flow (i.e., flux). In contrast, nanoporous flat sheet membrane structures can facilitate high flux, but at the price of generally unfavorable surface area-to-volume ratios.[18] Thus, there exists a trade-off between ion binding capacity per unit volume and fluid flow. Managing this dichotomy constitutes an all-but-unmet challenge.

To date, strategies to overcome the capacity-flux paradigm have relied on clever geometric designs across the nano- to macroscale continuum. This includes microstructuring (e.g., corrugating),[19−22] combining multiple flat sheet membranes

Received: November 10, 2023
Revised: January 5, 2024
Accepted: January 8, 2024
Published: February 1, 2024

https://doi.org/10.1021/jacs.3c12635
J. Am. Chem. Soc. 2024, 146, 4078−4086

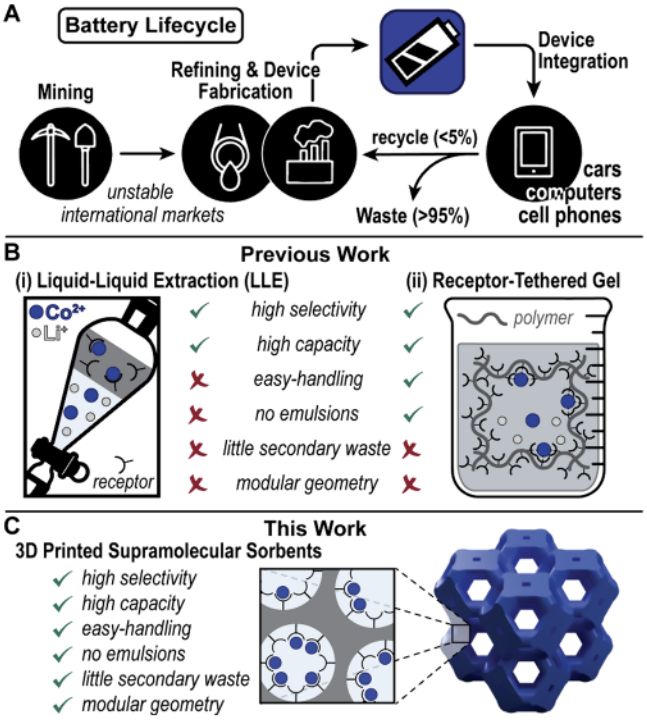

Figure 1. Life cycle of critical materials for batteries and methods for recycling. (A) Typical lifecycle of cobalt for batteries. (B) Contemporary strategies for critical material recovery by means of (i) liquid−liquid extractions with Cyanex-272 to recover $CoCl_2$ and (ii) using organogels containing tethered receptors to recover LiCl. (C) Present work where 3D-printed structured supramolecular sorbents selectively bind and release $CoCl_2$.

into a single module (cartridge),[23−25] and curling hollow-fiber membranes.[26−29] The apparent importance of multiscale geometric control for high performance ion separations has put 3D printing in the spotlight as an attractive manufacturing tool for this application. In turn, recent studies have emerged where 3D-printed scaffolds have been used in gas separations,[30] nuclear wastewater treatment,[31] Au, Pd, Pt, and Co electronic waste recycling,[32,33] oil extractions from contaminated water,[34] and perchlorate remediation.[35] Despite these impressive advances, the combination of supramolecular receptors, nanoporous materials, and high-resolution 3D printing for separations, to our knowledge, has not been considered in the context of metal ion recognition. It is thus an open question whether such an approach can be used to produce sorbents for critical metal cation capture. As detailed below, we have now found that digital light processing (DLP) 3D printing can be leveraged as a high resolution, scalable,[36] and low-waste tool to fabricate hierarchical sorbents for cobalt recycling (Figure 1C).

The present approach relies on polymerization-induced phase separation (PIPS) from a photocurable resin that serves to install nanopores during the DLP printing process. To allow for cobalt capture, a methacrylate functionalized tetradentate bisdicyclohexyl acetamide (BDCA) ligand was synthesized and directly incorporated into the 3D prints. Based upon our prior studies using glycolamide-based receptors, such as BDCA, for solvent-polarity-dependent binding of lithium,[12] we postulated that cobalt would also bind with BDCA due to the similarities in coordination preferences between the two ions. Indeed, binding and release of cobalt chloride was demonstrated using ethanol and water as "green" solvents for polarity switching. Furthermore, the influence of nanopore size and microscopic lattice geometry were systematically examined with respect to binding capacity and rate of adsorption, showcasing the utility of structured sorbents in critical material recycling.

RESULTS AND DISCUSSION

Receptor Synthesis. The porous sorbents described herein were prepared from a resin mixture containing a support monomer, receptor comonomer, and porogens (Figure 2A). A copolymerization approach was chosen to install the receptor in one step, ensuring incorporation with precise control over content via feed ratios, while mitigating the presence of unreacted functional groups that would occur if using a post-polymerization strategy.[37] The BDCA receptor was selected for Co^{2+} recycling given its precedent to bind and release $LiPF_6$ with high selectivity in acetonitrile,[12] along with the known affinity of glycolamides for transition metals.[38,39] To start, a polymerizable methacrylate handle was installed on the BDCA receptor to enable copolymerization with commercially available acrylate monomers commonly employed as resins for 3D printing. This was accomplished by reacting *tert*-butoxycarbonyl (BOC) protected 2-aminopropane-1,3-diol (**1**) with 2-bromo-*N*,*N*-dicyclohexylacetamide (**2**) in the presence of sodium hydride to generate the corresponding BOC-protected BDCA (**3**) (Scheme 1). Subsequent BOC deprotection with trifluoroacetic acid followed immediately by amide formation with methacryloyloxyethyl succinate (MA-OSu) provided the desired BDCA-methacrylate (BDCA-MA) monomer (Scheme 1). Copolymerization between BDCA-MA and carbitol acrylate (model monomer) initiated by phenylbis-(2,4,6-trimethylbenzoyl)phosphine oxide (BAPO) upon exposure to 405 nm light provided good receptor incorporation as desired (Figure S1). This proved true even though NMR spectroscopic analyses revealed that BDCA-MA reacted slightly faster than the carbitol acrylate.

Polymerization-Induced Phase Separation. Inspired by work from Levkin and co-workers[40] on 3D printing nanoporous structures via PIPS, we developed an analogous resin that incorporates BDCA-MA. Using tripropylene glycol diacrylate (TPGDA) as the support material, 1-decanol (dec) and cyclohexanol (cyc) as porogens, and BAPO as the photoinitiator, PIPS was evaluated for a range of monomer to porogen ratios, as well as the 1-decanol to cyclohexanol ratios (Figure 2A).

To correlate composition to phase separation, films were cast between glass slides with 75 μm spacers, irradiated with a 405 nm LED (5.0 mW/cm^2) for 120 s, washed with acetone to remove porogens and residual monomer, and dried in a vacuum oven overnight. The transmittance of each film was then measured and used to construct a ternary phase separation diagram using poly(TPGDA) prepared without porogens as a baseline (Figure 2B and Figure S2). A reduction in transmittance was taken as an indication of phase separation due to light scattering arising from nanoscale features. Therefore, transmittance below ∼unity was deemed as evidence for effective PIPS. On this basis, it was concluded that resins containing 50 wt ⊠ TPGDA relative to porogen resulted in phase separation, while higher TPGDA contents (lower porogen concentrations) did not phase separate (Figure 2B). Qualitatively, varying the cyclohexanol to 1-decanol ratios while maintaining a constant TPGDA content of 50 wt ⊠ provided good control over the extent of PIPS, as indicated by

https://doi.org/10.1021/jacs.3c12635
J. Am. Chem. Soc. 2024, 146, 4078−4086

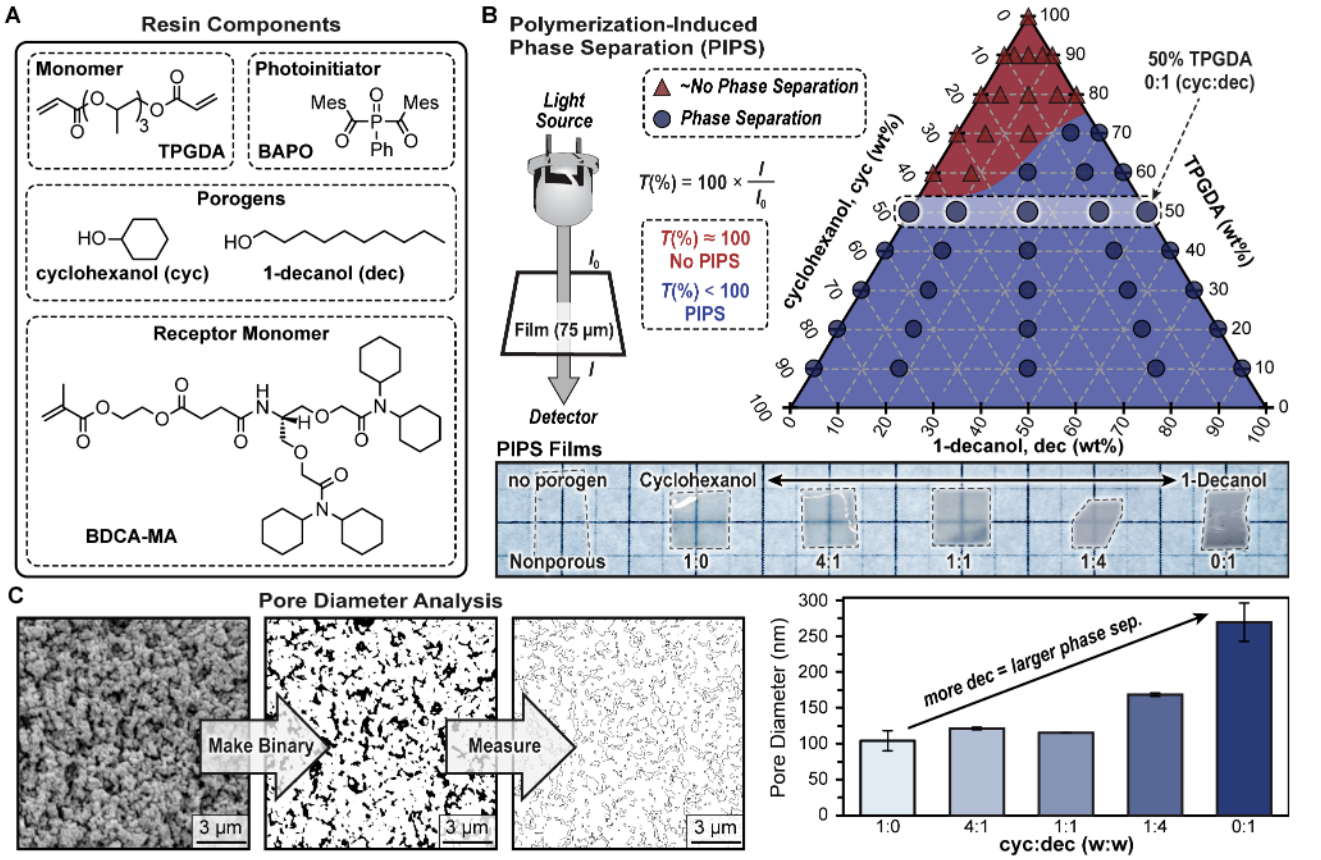

Figure 2. Resin formulation and corresponding polymerization-induced phase separation (PIPS). (A) Chemical structures of resin components. (B) Depiction of film transmittance measurements and ternary plot showing the resin formulations that either do or do not undergo PIPS. Selected resin formulations containing 1:1 porogens to TPGDA are indicated. Image of the films prepared with a range of cyclohexanol to 1-decanol ratios and the no-porogen control. (C) Representative image and analysis for a 0:1 cyclohexanol to 1-decanol sample using SEM and ImageJ. Bar chart with average pore diameters (nm) for resins prepared with 1:0 to 0:1 cyclohexanol/1-decanol ratios. Pore diameters are averages from three trials with error bars representing one standard deviation from the mean.

Scheme 1. Synthesis of bis-dicyclohexylacetamide methacrylate (BDCA-MA)[a]

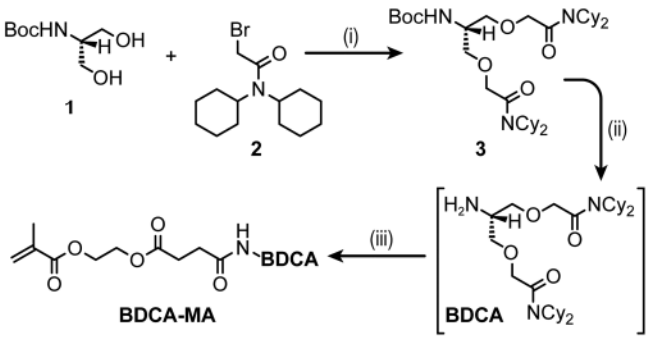

[a]Conditions: (i) NaH, THF, 85°C; (ii) CF_3COOH, CH_2Cl_2; (iii) methacryloyloxyethyl succinate (MA-OSu), NEt_3, CH_2Cl_2, 80°C.

a decrease in transmittance (increase in opacity) as the ratio decreased (i.e., more 1-decanol; Figure 2B, images). Thus, going forward we chose to use 50 wt % porogen relative to TPGDA (Tables S1 and S2). The same samples were prepared using critical point drying (CPD) instead of vacuum oven drying to mitigate pore collapse. Scanning electron microscopy (SEM) was performed to determine pore sizes following a previously reported image analysis protocol.[40−42] This analysis revealed pore diameters of 100 ± 10, 122 ± 2, 115 ± 1, 168 ± 2, and 270 ± 30 nm for cyclohexanol/1-decanol ratios of 1:0, 4:1, 1:1, 1:4, and 0:1, respectively (Figure 2C and Figures S3 and S4). These results served to corroborate the qualitative observation of opacity, where increasing the amount of 1-decanol relative to cyclohexanol was found to produce larger phase separated domains and bigger pores upon removal of the porogens. The incorporation of BDCA-MA into the polymer network using this method was next confirmed using elemental analysis and attenuated total reflectance (ATR) Fourier transform infrared (FTIR) spectroscopy. By increasing the receptor feed from 0 to 5 mol % relative to TPGDA, the resultant polymers were found to contain nitrogen contents of 0.113 ± 0.006% to 0.57 ± 0.02%, respectively (Table S3). This correlates well with the theoretical loading levels (nitrogen content = 0.13 and 0.60%, respectively). These findings were thus taken as evidence that receptor loading had been successfully achieved. ATR-FTIR spectroscopy of the polymers further confirmed the incorporation of BDCA-MA as inferred from the presence of secondary amine and amide signatures at 3270 cm^{-1} (N−H stretching) and 1639 cm^{-1} (C O stretching), respectively (Figure S7). On this basis, we conclude that light-driven PIPS from resins containing BDCA-MA constitutes a viable strategy for the preparation of materials with tunable pore size and receptor content.

Digital Light Processing (DLP) 3D Printing. Polymeric objects were prepared using digital light processing (DLP) 3D

https://doi.org/10.1021/jacs.3c12635
J. Am. Chem. Soc. 2024, 146, 4078−4086

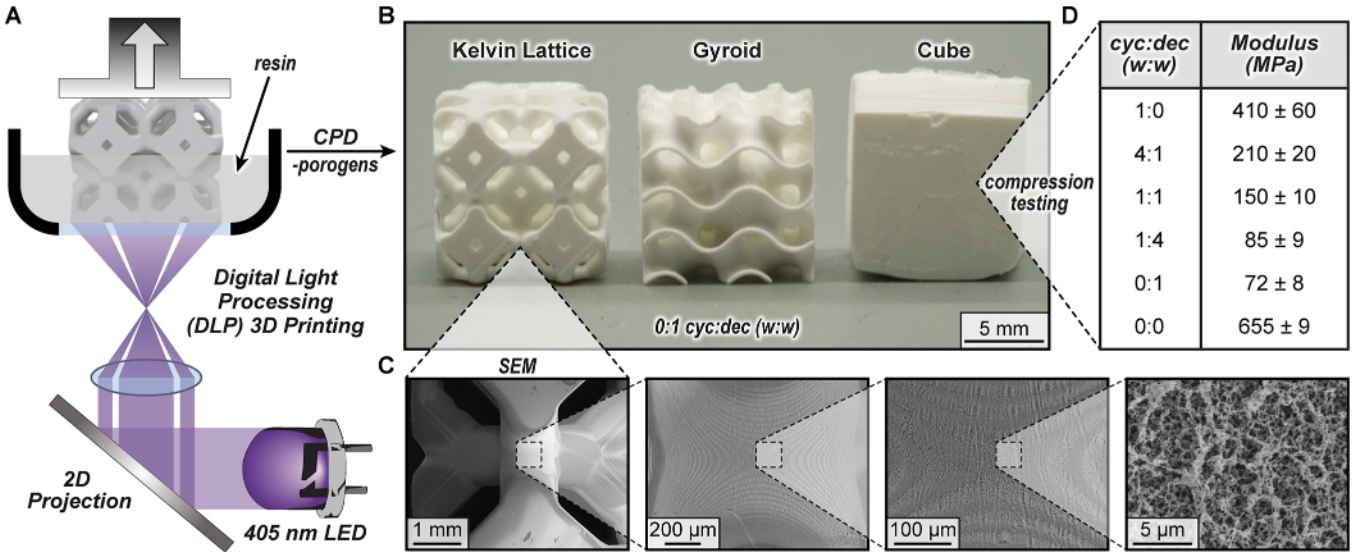

Figure 3. Digital light processing (DLP) 3D printing and analyses. (A) Schematic representation of DLP 3D printing that contains a light emitting diode (LED), digital mirror device (DMD), vat with liquid resin, and build platform. (B) Representative images of printed and critical point dried (CPD) kelvin lattice, gyroid, and cube (10 mm × 10 mm × 10 mm), prepared from resins containing a 0:1 cyclohexanol/1-decanol ratio. (C) Scanning electron microscopy (SEM) images of the kelvin lattice (10 mm × 10 mm × 10 mm) prepared with 0:1 cyclohexanol/1-decanol ratio. (D) Average compression testing elastic moduli of cubes (5 mm × 5 mm × 5 mm) prepared with different porogen ratios. Moduli values are averages from three trials with one standard deviation from the mean provided.

printing, which is a layer-by-layer stereolithography technique that provides an attractive combination of build speed, feature resolution,[43] and isotropic mechanical properties.[44] All objects were produced using the following print settings: bottom-up LED exposure with a central wavelength of 405 nm, intensity of 8.6 mW/cm^2, and 1 s irradiation time per 25 μm layer (Figure 3A). Printed objects were soaked in ethanol to remove residual resin components. The resulting structures could be used directly for ion sorption experiments (i.e., without drying); however, CPD was employed to characterize structure and enable the gravimetric analyses used to quantify ion capacity (vide infra).[40] The accessible surface areas of dried samples prepared as printed cylinders (3 mm × 22 mm) were estimated using the Brunauer−Emmett−Teller (BET) approach with N_2 as the probe gas. These studies revealed a general trend of increasing surface area from 20.3 ± 0.3 to 45.4 ± 0.3 m^2/g as the pore size decreased from 270 ± 30 nm to 122 ± 2 nm for samples prepared from resins containing cyclohexanol to 1-decanol ratios of 0:1 and 4:1, respectively (Table S4 and Figure S8). These surface area and pore size values are on the same order of magnitude as those previously reported for materials prepared by PIPS.[40] Notably, the samples with the smallest pores (∼100 nm as measured on the films using SEM), had a lower measured surface area relative to those having the next smallest pores (∼120 nm). This finding is attributed to the presence of phase mixed regions or isolated pores (Figure S5).[45] Finally, density measurements of 3D-printed cubes revealed porosity values that increased from 24 ± 2 to 50.6 ± 0.9% upon increasing the pore size from ∼100 to 300 nm (Table S5). To test whether the present additive manufacturing approach would allow access to complex microarchitectures, three structures were produced all having 10 mm × 10 mm × 10 mm outer dimensions, namely cube, kelvin lattice, and gyroid.[46] Such geometric control has the potential to enable production of mechanically robust sorbents with improved longevity and reuse, along with the ability to maximize capacity and flux.[47] The structures were produced with high feature fidelity, as demonstrated by hole diameters of ∼500 μm in the kelvin lattice and wall thicknesses of ∼375 μm in the gyroids (Figure 3B). This printing process thus provided hierarchical structures that span the nm to mm length scales as determined from SEM imaging that revealed nanoporous voids, micrometer-steps analogous to those in corrugated membranes,[21,22] and millimeter lattices (Figure 3C). The influence of pore size on the mechanical integrity was also examined by carrying out uniaxial compression tests on 5 mm × 5 mm × 5 mm nanoporous cubes. These studies revealed elastic moduli (E) ranging from 410 ± 60 to 72 ± 8 MPa for 100% cyclohexanol (∼100 nm pores) to 100% 1-decanol (∼300 nm pores), respectively (Figure 3D and Figure S9). Thus, we conclude that the stiffness of the present printed structures could be tuned by controlling porosity. This ability, in turn, provides a mechanism to design sorbents appropriate to meet the demands of a particular separations process (e.g., specific fluid pressures).

Cobalt(II) Chloride Binding. Although attempts to grow single crystals of BDCA-$CoCl_2$ were unsuccessful, a diffraction-grade BDCA-$NiCl_2$ crystal was obtained via vapor diffusion from diethyl ether into an ethyl acetate solution containing BDCA-$NiCl_2$ and served as a proxy. The resulting cluster-like structure revealed the presence of octahedral complexes, chloride-bridged bimetallic complexes, and a tetrachlorometallate (Figure S11). In solution, these coordination complexes can exist in equilibrium with multiple species.[48−50] This complexity precluded the attainment of reliable binding constants for the free receptors. However, for the case of immobilized receptors, the relative affinities could be inferred from Freundlich constant and exponents (vide infra).

The Co^{2+} binding profiles of 3D-printed sorbents were measured in so-called "green" solvents, namely ethanol (EtOH), isopropyl alcohol (IPA), and water (H_2O), to determine the most selective analyte binding and release environments. Kelvin lattices (10 mm × 10 mm × 10 mm) containing 5 mol % BDCA receptor and ∼120 nm pores (from

https://doi.org/10.1021/jacs.3c12635
J. Am. Chem. Soc. 2024, 146, 4078−4086

cyclohexanol/1-decanol 1:1) were placed in a container with a defined concentration (~mM) of cobalt chloride ($CoCl_2$) or lithium chloride (LiCl) (Figure 4A). After allowing to stand for

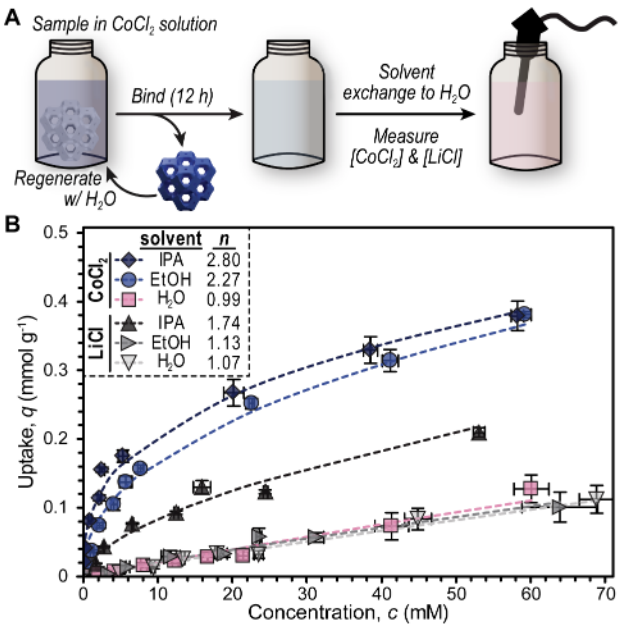

Figure 4. Ion binding and selectivity for 3D-printed kelvin lattices containing 5 mol % BDCA and ~120 nm pores (from cyclohexanol/1-decanol 1:1). (A) Illustration of the process used to determine ion binding via conductivity measurements. (B) Binding isotherms for $CoCl_2$ and LiCl in various solvents, with uptake provided as millimoles of ions relative to grams of bulk sorbent. Dashed lines represent fits to a nonlinear Freundlich model. Symbols represent averages from three trials with error bars representing one standard deviation from the mean.

12 h to reach equilibrium, the 3D-printed structures were removed, the initial solvents were exchanged for water, and the conductivity values measured to determine ion concentrations by comparison to calibration curves (Figure S12). The experimental binding profiles were fit to nonlinear Freundlich isotherms with R^2 values exceeding 0.95. In these models, correction factors (n) provide insights into the ion binding interactions. Specifically, when $n^{-1} < 1$, binding is favorable, while $n^{-1} > 1$ indicates unfavorable binding.[51] For $CoCl_2$, strong binding in IPA and EtOH was observed, with n values of 2.80 and 2.27, respectively (Figure 4B). Conversely, weak binding of $CoCl_2$ in H_2O was observed, with an n value of 0.99. This difference allowed EtOH or IPA to be used as solvents for effective $CoCl_2$ binding, whereas treatment with H_2O could be used to effect Co^{2+} release. Ultimately, we think that this solvent polarity switching in combination with appropriately 3D-printed receptor-containing materials could be used for cobalt recycling.

The BDCA ligand has affinity for lithium salts. Given this propensity, and the presence of Li^+ in acid leachate from lithium-ion batteries[52] (along with Co^{2+}), we next chose to examine the Li^+ binding capabilities of the present BDCA-MA based 3D-printed sorbents. These studies were further motivated by an appreciation of the difficulty in selectively separating these two ions (Co^{2+} vs Li^+) using contemporary strategies.[53,54] The adsorption isotherms of LiCl in IPA and EtOH provided n values of 1.74 and 1.13, respectively, which were both lower than those for $CoCl_2$ (Figure 4B). The affinity of the BDCA ligand for manganese- and nickel-salts was also examined given their increasing presence in lithium-ion battery cathodes. The Freundlich isotherms revealed that BDCA had a moderately higher affinity for $CoCl_2$ over $NiCl_2$ in EtOH (n = 2.27 vs 2.07), while a much lower affinity for $MnCl_2$ in EtOH was observed (n = 1.14, Figure S13). These results lead us to suggest that the 3D-printed sorbents can provide selectivity for Co^{2+} over Li^+ and Mn^{2+} in alcohol solvents. Based on the relatively large difference in binding affinity in EtOH, along with its reduced toxicity compared to IPA, further experiments were performed using EtOH as the solvent.

Next, the fundamental binding kinetics and capacities of the structured sorbents as a function of nanoporosity and microstructure were examined using the kelvin lattice. The blue appearance of tetrahedral cobalt complexes provides a distinct visual queue for adsorption and provides a colorimetric sensor for qualitatively assessing the extent of BDCA-$CoCl_2$ complex formation (Figure 5A). The colored sorbent was characterized using SEM and energy-dispersive X-ray (EDX) spectroscopy to determine the elemental composition. Mapping of cobalt and chlorine showed a similar homogeneous spatial distribution and provided a ratio of ~1:2 for Co/Cl. This elemental ratio is taken as evidence that the bound cobalt is in the 2+ oxidation state.

The influence of nanopore size on the rate of cobalt uptake was also determined. We hypothesized that increasing the pore size would lead to an increase in the rate of diffusive transport, and therefore uptake. To test this conjecture, kelvin lattices with pore sizes ranging from ~100 nm (cyclohexanol only) to ~300 nm (1-decanol only) were prepared with 5 mol % BDCA, along with nonporous controls (Table S2). The rate of uptake was tracked by monitoring the change in absorption at 659 nm (tetrahedral cobalt complex) of the EtOH solution containing the printed object as a function of time. Changes in the $CoCl_2$ concentration were determined from a calibration curve (Figures S14 and S15). On this basis, we were able to confirm that the rate of uptake increased with pore size as predicted (Figure 5B). Specifically, samples with the largest pores (~300 nm) exhibited a pseudo-first-order rate constant (k_1) of $8 \pm 1 \times 10^{-2}$ min^{-1}. Conversely, the samples containing the smallest pores (~100 nm) displayed a k_1 of $4 \pm 2 \times 10^{-2}$ min^{-1}. This finding provides support for the suggestion that the $CoCl_2$ uptake in these samples is diffusion limited.

The influence of receptor loading on $CoCl_2$ equilibrium capacity was then examined for kelvin lattices containing nanopores of intermediate size (~120 nm, from a 1:1 mixture of cyclohexanol/1-decanol). For these studies, samples were soaked in 25 mM $CoCl_2$ solutions (EtOH) and aliquots were removed after 48 h and the total uptake determined spectroscopically. As expected, increasing the BDCA receptor loading from 0 to 5 mol % led to a corresponding increase in uptake, as noted by the visual increase in blue color (Figure 5C). Specifically, for 0, 1, 2.5, and 5 mol % BDCA-MA uptake values of -0.7 ± 0.9, 3.5 ± 0.8, 9.5 ± 0.4, and 12 ± 2 mg·g^{-1} were recorded, respectively. These uptake values correspond to 80 ± 20%, 89 ± 5%, and 60 ± 8% of the theoretical maximum binding capacity. Analogous studies involving samples with the smallest nanopores (~100 nm) and 2.5 mol % BDCA-MA produced an uptake value of 5 ± 1 mg·g^{-1}, which corresponds to a 50 ± 10% binding capacity (Figure 5C). As expected, increasing the nanopore size to ~300 nm while maintaining 2.5

https://doi.org/10.1021/jacs.3c12635
J. Am. Chem. Soc. 2024, 146, 4078−4086

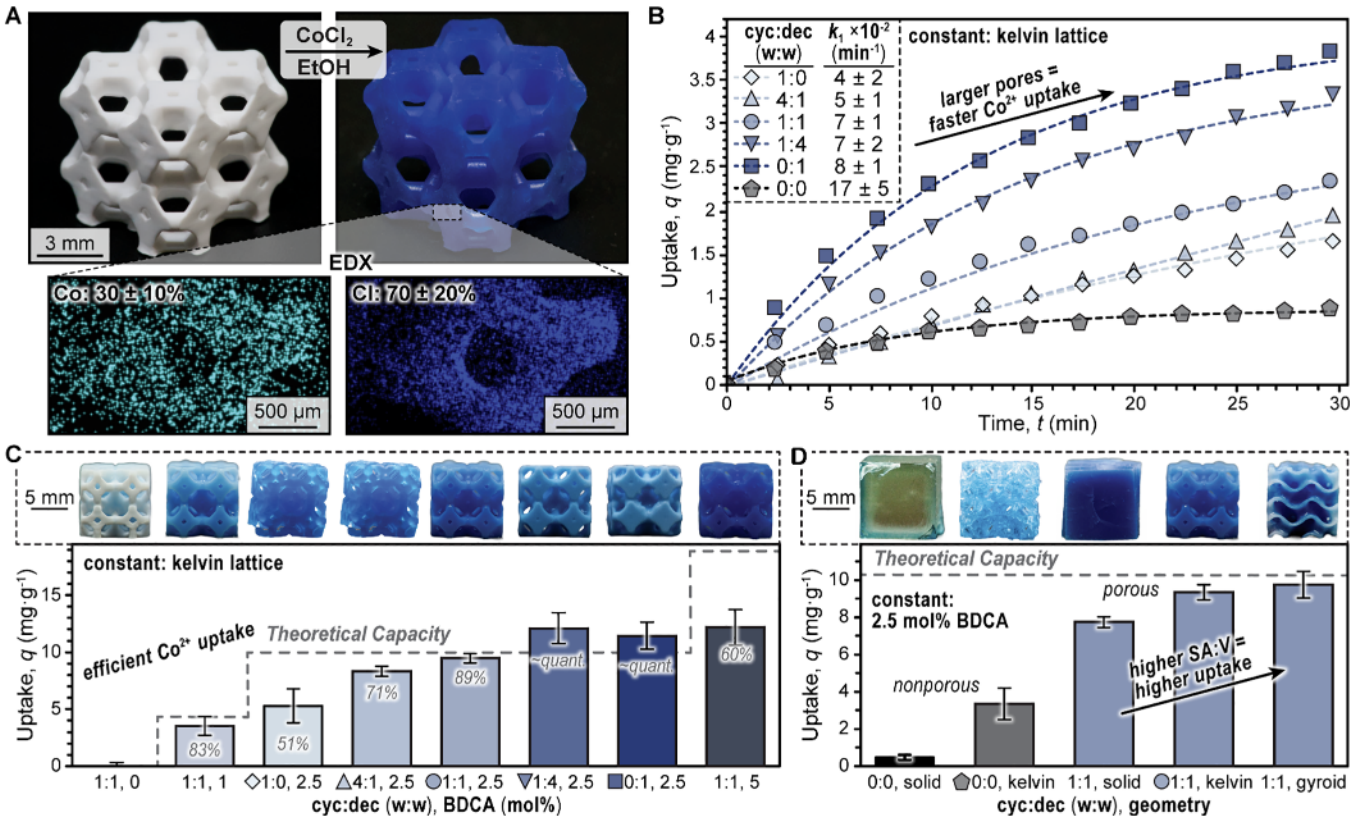

Figure 5. Adsorption of $CoCl_2$ to BDCA containing 3D-printed sorbents. (A) Digital camera images of a kelvin lattice comprising 5 mol % BDCA before and after $CoCl_2$ binding in a 25 mM EtOH solution (top). SEM-EDX mapping images for Co and Cl on the sorbent surface (bottom). (B) Representative kinetic adsorption isotherms measured using UV−vis absorption spectroscopy. Symbols provided are indexed for clarity and the dashed lines represent a nonlinear pseudo-first order fit. Rate constants (k_1) were determined from an average of three trials with error representing one standard deviation from the mean. (C) Equilibrium uptake as a function of receptor loading and pore size for kelvin lattices. (D) Equilibrium uptake as a function of 3D microstructure. Data provided are averages from three trials with error bars representing one standard deviation from the mean. SA:V, surface area to volume ratio.

mol % BDCA led to nearly 100% binding (Figure 5C and Figure S18).

Finally, the influence of microstructure on the $CoCl_2$ capacity and rate of uptake was examined (Figure 5D). Samples with cube, kelvin lattice, and gyroid geometries having nanopores of intermediate size (~120 nm, from a 1:1 mixture of cyclohexanol and 1-decanol) along with a nonporous cube control were tested following the same soaking and UV−vis absorption spectroscopy protocols used above. Geometries with larger surface-area-to-volume ratios (gyroid > kelvin lattice > cube > nonporous kelvin lattice > nonporous cube) were found to result in higher capacity and faster uptake rates (Figure 5D and Figure S16). Specifically, uptake values of 94 ± 7%, 91 ± 4%, 75 ± 3%, 32 ± 8%, and 5 ± 1% relative to the theoretical maximum capacity were measured for the gyroid, kelvin lattice, cube, and nonporous cube, respectively. These results demonstrate that the surface area-to-volume ratio influences the binding properties. Thus, performance can be related directly to both the nano- and microscale geometries that, in turn, are readily controllable via the present 3D printing approach.

To extend the present platform to real world critical material recycling requires both the ability to bind ("catch") and release the desired ion, and to do so reproducibly over many cycles. We tested this capability via "green" solvent cycling between EtOH and H_2O with a 5 mol % BDCA-containing kelvin lattice having ~120 nm pores (prepared from a 1:1 cyclohexanol to 1-decanol porogen mixture) (Figure 6A). Samples were placed into a stock solution of $CoCl_2$ in EtOH (18.76 mM), allowed to bind for 12 h, and then removed. The conductivity of the stock solution was measured to determine the amount of bound $CoCl_2$ relative to a calibration curve (Figure S12). This revealed a 78 ± 2% binding capacity, which was comparable to that obtained using UV−vis absorption spectroscopy on an analogous sample (5 mol % BDCA, 120 nm pores, kelvin lattice) after a 48 h soak to allow equilibrium to be reached (60 ± 8% binding, Figure 5C). Subsequently, the Co-laden sorbent was placed in pure H_2O for 12 h and the conductivity was measured to assess the amount of released $CoCl_2$ based on a calibration curve (Figure S12). Notably, 90 ± 1% of the bound $CoCl_2$ was released after the first cycle, which was further supported by a visual loss in sorbent color (i.e., blue to white) (Figure 6A). The release of $CoCl_2$ is attributed to an increase in ion−solvent interaction strength that follows the spectrochemical series[55] for increasing polarity in going from ethanol to water. Repeating this process with the regenerated sorbent over a total of 5 cycles revealed no statistically significant change in binding or release capacity. Additionally, no change to the morphology (Figure S6) or elastic moduli of representative samples post cycling was observed (Figure S10). On this basis we conclude that the present system provides for good reproducibility when subject to repeated use.

https://doi.org/10.1021/jacs.3c12635
J. Am. Chem. Soc. 2024, 146, 4078−4086

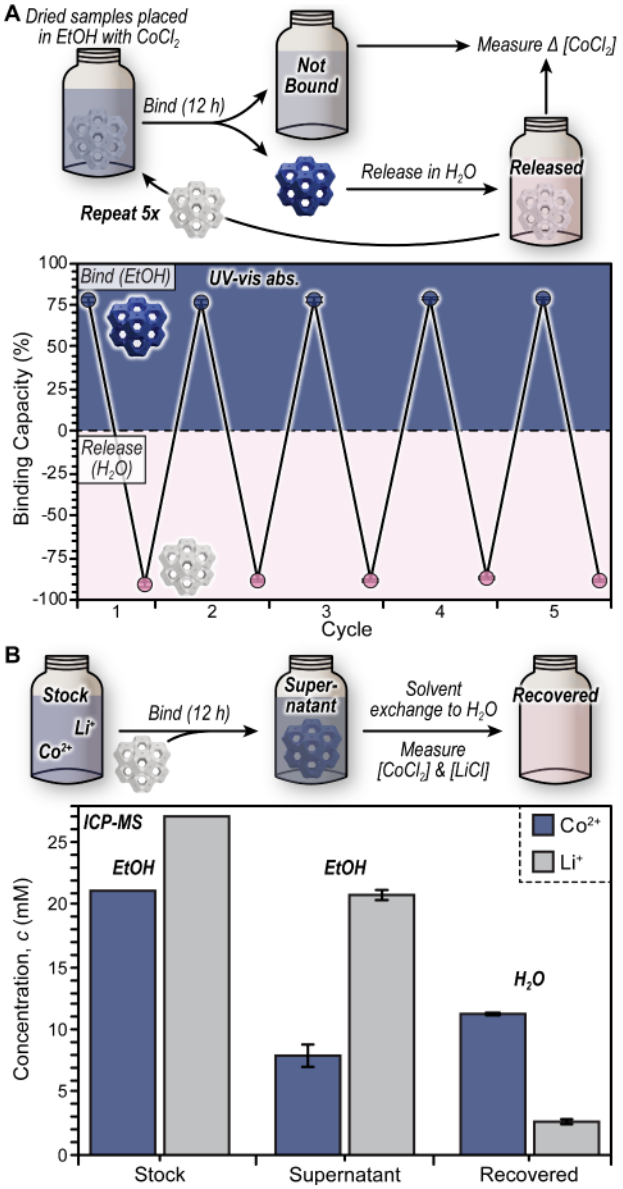

Figure 6. Reusability and selectivity of 5 mol % BDCA-containing 3D-printed kelvin lattice sorbents when tested for cobalt binding and release. (A) Illustration and experimental data for cyclic catch-and-release experiments. Release percentage is relative to the amount of $CoCl_2$ bound in that same cycle. (B) Illustration and experimental data for Co^{2+} over Li^+ selectivity. All data are the averages of three independent trials with error bars representing one standard deviation from the mean.

$LiCoO_2$ is currently the most common cathode material in portable batteries.[56] Recycling of these batteries includes an early stage acid (e.g., HCl) leaching step. This produces a mixture of Co^{2+} and Li^+ from which it is notoriously difficult to separate out the individual ions. We thus sought to determine the selectivity of the present sorbents for Co^{2+} over Li^+. With this goal in mind, we prepared a simulated leachate solution containing LiCl and $CoCl_2$ in EtOH (2 mL) and placed three distinct 5 mol % BDCA-containing 3D-printed kelvin lattices (230 mg sample, ~120 nm pores) in the mixed ion solution (Figure 6B). Inductively coupled plasma mass spectrometry (ICP-MS) analysis revealed initial concentrations of 27.0 and 21.1 mM for Li^+ and Co^{2+}, respectively. After soaking the sorbents in the solution for 12 h, the now blue samples were removed, rinsed with EtOH, and then placed in pure H_2O (2 mL) for 12 h to release the bound ions. At the end of this procedure, the initial ethanol phase was found to contain a considerably higher ratio of Li^+ to Co^{2+} with concentrations of 20.7 ± 0.4 mM and 7.9 ± 0.9 mM being recorded for Li^+ and Co^{2+}, respectively (Figure 6B). Conversely, the final aqueous phase was found to contain 2.6 ± 0.2 mM of Li^+ and 11.2 ± 0.1 mM of Co^{2+}. This corresponds to a 5.6× reduction in the Li^+ to Co^{2+} ratio, from 1.28 to 0.23. The selectivity of the 3D-printed support for Co^{2+} over Li^+ corresponds to the binding isotherms in ethanol (see Figure 3B) and is taken as evidence that the BDCA-containing 3D-printed kelvin lattices bind Co^{2+} more strongly than Li^+. More broadly, these findings lead us to suggest that 3D-printed nanoporous polymer sorbents, such as those described here, may enable effective lithium-ion battery recycling with minimal secondary waste generation.

CONCLUSION AND OUTLOOK

In this study, we detail the preparation and testing of a 3D-printed hierarchical nanoporous sorbent platform for cobalt recycling. A novel methacrylate-functionalized bisdicyclohexyl acetamide receptor was synthesized and copolymerized with a commercial diacrylate and porogens to form nanoporous materials via photoinitiated polymerization-induced phase separation. Digital light processing allowed the 3D printing of objects with defined microstructures. The influence of nano- and microscale features on the $CoCl_2$ uptake rate and binding capacity in ethanol was systematically examined. A direct positive correlation with higher surface area-to-volume ratios was found. Furthermore, efficient release of captured $CoCl_2$ in a benign aqueous environment was demonstrated, along with excellent sorbent reusability through five catch-and-release cycles with no apparent loss in performance being observed. Finally, selective binding of $CoCl_2$ over LiCl was achieved in simulated ethanolic battery leachates.

The present results demonstrate the potential of this platform in the context of cobalt recycling from spent lithium-ion batteries. Given its modularity, low cost, and minimal waste generation, we propose that the present strategy can be generalized to allow for the beneficiation and recycling of critical materials. Current efforts are devoted to exploring this possibility.

ASSOCIATED CONTENT

Supporting Information

The Supporting Information is available free of charge at https://pubs.acs.org/doi/10.1021/jacs.3c12635.

Experimental (materials, instrumentation, and synthesis) and characterization details (PDF)

Accession Codes

CCDC 2313514 contains the supplementary crystallographic data for this paper. These data can be obtained free of charge via www.ccdc.cam.ac.uk/data_request/cif, or by emailing data_request@ccdc.cam.ac.uk, or by contacting The Cambridge Crystallographic Data Centre, 12 Union Road, Cambridge CB2 1EZ, UK; fax: +44 1223 336033.

AUTHOR INFORMATION

Corresponding Authors

Zachariah A. Page − *Department of Chemistry, The University of Texas at Austin, Austin, Texas 78712, United States;*

https://doi.org/10.1021/jacs.3c12635
J. Am. Chem. Soc. 2024, 146, 4078−4086

orcid.org/0000-0002-1013-5422; Email: zpage@cm.utexas.edu

Jonathan L. Sessler − *Department of Chemistry, The University of Texas at Austin, Austin, Texas 78712, United States;* orcid.org/0000-0002-9576-1325; Email: sessler@cm.utexas.edu

Authors

Keldy S. Mason − *Department of Chemistry, The University of Texas at Austin, Austin, Texas 78712, United States;* orcid.org/0000-0003-2481-4570

Sheng-Yin Huang − *Department of Chemistry, The University of Texas at Austin, Austin, Texas 78712, United States;* orcid.org/0000-0002-3278-3826

Samuel K. Emslie − *Department of Chemistry, The University of Texas at Austin, Austin, Texas 78712, United States*

Qian Zhang − *Department of Chemistry, The University of Texas at Austin, Austin, Texas 78712, United States*

Simon M. Humphrey − *Department of Chemistry, The University of Texas at Austin, Austin, Texas 78712, United States;* orcid.org/0000-0001-5379-4623

Complete contact information is available at: https://pubs.acs.org/10.1021/jacs.3c12635

Author Contributions

†K.S.M. and S.-Y.H. contributed equally to this work.

Notes

The authors declare no competing financial interest.

■ ACKNOWLEDGMENTS

The authors acknowledge primary support from the National Science Foundation under grant no. DMR-2045336 (K.S.M., Z.A.P.). Partial support was provided by the Robert A. Welch Foundation under grant Nos. F-2007 (Z.A.P.), F-0018 (J.L.S.) and F-1738 (S.M.H.), the Research Corporation for Science Advancement under grant no. 28184 (Z.A.P.), and the U.S. Department of Energy Office of Basic Energy Sciences (grant no. DE-SC0024393 to J.L.S.). The authors acknowledge the use of shared research facilities supported in part by the Texas Materials Institute and the Center for Dynamics and Control of Materials (NSF MRSEC) under grant no. DMR-1720595. The authors thank Atlantic Microlab for carrying out elemental analysis. The authors thank Vincent Garcia for his generation of kelvin and gyroid lattice CAD models. The authors thank Dr. Yun-Ho Jang at MonoPrinter for his support with the custom LCD & DLP 3D printers and associated MonoWare software.

■ ABBREVIATIONS

DLP, digital light processing; PIPS, polymerization-induced phase separation; BDCA, bis-dicyclohexyl acetamide; BDCA-MA, methacrylate functionalized bisdicyclohexyl acetamide; DRC, Democratic Republic of Congo; LLE, liquid−liquid extraction; EtOH, ethanol; BOC, *tert*-butoxycarbonyl; BAPO, phenylbis(2,4,6-trimethylbenzoyl)phosine oxide; TPGDA, tripropylene glycol diacrylate; dec, 1-decanol; cyc, cyclohexanol; CPD, critical point drying; SEM, scanning electron microscopy; ATR, attenuated total reflectance; FTIR, Fourier transform infrared; BET, Brunauer−Emmett−Teller; IPA, isopropanol; EDX, energy-dispersive X-ray; ICP-MS, inductively coupled plasma mass spectroscopy

■ REFERENCES

(1) Upadhyaya, G. S. Materials Science of Cemented Carbides — an Overview. *Mater. Des* **2001**, *22* (6), 483−489.

(2) Coutsouradis, D.; Davin, A.; Lamberigts, M. Cobalt-Based Superalloys for Applications in Gas Turbines. *Materials Science and Engineering* **1987**, *88* (C), 11−19.

(3) Sun, X.; Shi, Q.; Hao, X. Supply Crisis Propagation in the Global Cobalt Trade Network. *Resour Conserv Recycl* **2022**, *179*, 106035.

(4) Igogo, T. America's Strategy to Secure the Supply Chain for a Robust Clean Energy Transition, 2022. https://www.energy.gov/policy/articles/americas-strategy-secure-supply-chain-robust-clean-energy-transition (accessed 2023−10−25).

(5) Jacoby, M. It's Time to Get Serious about Recycling Lithium-Ion Batteries. *C EN Global Enterp.* **2019**, *97* (28), 29−32.

(6) Chen, J.; Zhang, H.; Zeng, Z.; Gao, Y.; Liu, C.; Sun, X. Separation of Lithium and Transition Metals from the Leachate of Spent Lithium-Ion Battery by Extraction-Precipitation with p-Tert-Butylphenoxy Acetic Acid. *Hydrometallurgy* **2021**, *206*, 105768.

(7) Rodrigues, I. R.; Deferm, C.; Binnemans, K.; Riano, S. Separation of Cobalt and Nickel via Solvent Extraction with Cyanex-272: Batch Experiments and Comparison of Mixer-Settlers and an Agitated Column as Contactors for Continuous Counter-Current Extraction. *Sep Purif Technol.* **2022**, *296*, 121326.

(8) Sarangi, K.; Reddy, B. R.; Das, R. P. Extraction Studies of Cobalt (II) and Nickel (II) from Chloride Solutions Using Na-Cyanex 272.: Separation of Co(II)/Ni(II) by the Sodium Salts of D2EHPA, PC88A and Cyanex 272 and Their Mixtures. *Hydrometallurgy* **1999**, *52* (3), 253−265.

(9) Hirayama, Y.; Hinoue, M.; Tokumoto, H.; Matsuoka, A.; Noishiki, K.; Muto, A. Liquid-Liquid Extraction and Separation of Cobalt and Lithium Ions Using a Slug Flow Microreactor. *J. Chem. Eng. Jpn.* **2018**, *51* (3), 222−228.

(10) Aydogan, A.; Coady, D. J.; Lynch, V. M.; Akar, A.; Marquez, M.; Bielawski, C. W.; Sessler, J. L. Poly(Methyl Methacrylate)s with Pendant Calixpyrroles: Polymeric Extractants for Halide Anion Salts. *Chem. Commun.* **2008**, *12*, 1455−1457.

(11) Wang, H.; Jones, L. O.; Hwang, I.; Allen, M. J.; Tao, D.; Lynch, V. M.; Freeman, B. D.; Khashab, N. M.; Schatz, G. C.; Page, Z. A.; Sessler, J. L. Selective Separation of Lithium Chloride by Organogels Containing Strapped Calix[4]Pyrroles. *J. Am. Chem. Soc.* **2021**, *143* (48), 20403−20410.

(12) Huang, S.-Y.; Wang, H.; Celio, H.; Khashab, N. M.; Page, Z. A.; Sessler, J. L. Polystyrene-Supported Neutral Lithium Receptor for the Recovery of High-Purity LiPF6 from Simulated Degraded Electrolyte. *J. Mater. Chem. A* **2022**, *10*, 14788−14794.

(13) Lilac Solutions. New Extraction Methods. https://lilacsolutions.com/technology/ (accessed 2023-10−31).

(14) Kunin, R.; Barry, R. E. Carboxylic, Weak Acid Type, Cation Exchange Resin. *Ind. Eng. Chem.* **1949**, *41* (6), 1269−1272.

(15) Zainol, Z.; Nicol, M. J. Comparative Study of Chelating Ion Exchange Resins for the Recovery of Nickel and Cobalt from Laterite Leach Tailings. *Hydrometallurgy* **2009**, *96* (4), 283−287.

(16) Guibal, E.; Milot, C.; Tobin, J. M. Metal-Anion Sorption by Chitosan Beads: Equilibrium and Kinetic Studies. *Ind. Eng. Chem. Res.* **1998**, *37*, 1454−1463.

(17) Alexandratos, S. D.; Hussain, L. A. Bifunctionality as a Means of Enhancing Complexation Kinetics in Selective Ion Exchange Resins. *Ind. Eng. Chem. Res.* **1995**, *34* (1), 251−254.

(18) Ouimet, J. A.; Xu, J.; Flores - Hansen, C.; Phillip, W. A.; Boudouris, B. W. Design Considerations for Next-Generation Polymer Sorbents: From Polymer Chemistry to Device Configurations. *Macromol. Chem. Phys.* **2022**, *223*, 223.

(19) Bikel, M.; Culfaz, P. Z.; Bolhuis-Versteeg, L. A. M.; Pérez, J. G.; Lammertink, R. G. H.; Wessling, M. Polymeric Microsieves via Phase Separation Microfabrication: Process and Design Optimization. *J. Membr. Sci.* **2010**, *347*, 93−100.

(20) Papenburg, B. J.; Vogelaar, L.; Bolhuis-Versteeg, L. A. M.; Lammertink, R. G. H.; Stamatialis, D.; Wessling, M. One-Step

Fabrication of Porous Micropatterned Scaffolds to Control Cell Behavior. *Biomaterials* **2007**, *28* (11), 1998−2009.
(21) Vogelaar, L.; Barsema, J. N.; Van Rijn, C. J. M.; Nijdam, W.; Wessling, M. Phase Separation Micromolding - PSμM. *Adv. Mater.* **2003**, *15* (16), 1385−1389.
(22) Vogelaar, L.; Lammertink, R. G. H.; Barsema, J. N.; Nijdam, W.; Bolhuis-Versteeg, L. A. M.; Van Rijn, C. J. M.; Wessling, M. Phase Separation Micromolding: A New Generic Approach for Microstructuring Various Materials. *Small* **2005**, *1* (6), 645−655.
(23) Balster, J.; Punt, I.; Stamatialis, D. F.; Wessling, M. Multi-Layer Spacer Geometries with Improved Mass Transport. *J. Membr. Sci.* **2006**, *282* (1−2), 351−361.
(24) Balster, J.; Stamatialis, D. F.; Wessling, M. Towards Spacer Free Electrodialysis. *J. Membr. Sci.* **2009**, *341* (1−2), 131−138.
(25) Balster, J.; Stamatialis, D. F.; Wessling, M. Membrane with Integrated Spacer. *J. Membr. Sci.* **2010**, *360* (1−2), 185−189.
(26) Ghogomu, J. N.; Guigui, C.; Rouch, J. C.; Clifton, M. J.; Aptel, P. Hollow-Fibre Membrane Module Design: Comparison of Different Curved Geometries with Dean Vortices. *J. Membr. Sci.* **2001**, *181* (1), 71−80.
(27) Kaufhold, D.; Kopf, F.; Wolff, C.; Beutel, S.; Hilterhaus, L.; Hoffmann, M.; Scheper, T.; Schluter, M.; Liese, A. Generation of Dean Vortices and Enhancement of Oxygen Transfer Rates in Membrane Contactors for Different Hollow Fiber Geometries. *J. Membr. Sci.* **2012**, *423-424*, 342−347.
(28) Liu, S. H.; Luo, G. S.; Wang, Y.; Wang, Y. J. Preparation of Coiled Hollow-Fiber Membrane and Mass Transfer Performance in Membrane Extraction. *J. Membr. Sci.* **2003**, *215* (1−2), 203−211.
(29) Jani, J. M.; Wessling, M.; Lammertink, R. G. H. Geometrical Influence on Mixing in Helical Porous Membrane Microcontactors. *J. Membr. Sci.* **2011**, *378* (1−2), 351−358.
(30) Wu, J.; Zhu, X.; Yang, F.; Wang, R.; Ge, T. Shaping Techniques of Adsorbents and Their Applications in Gas Separation: A Review. *J. Mater. Chem. A Mater.* **2022**, *10* (43), 22853−22895.
(31) Halevi, O.; Chen, T. Y.; Lee, P. S.; Magdassi, S.; Hriljac, J. A. Nuclear Wastewater Decontamination by 3D-Printed Hierarchical Zeolite Monoliths. *RSC Adv.* **2020**, *10* (10), 5766−5776.
(32) Lahtinen, E.; Hänninen, M. M.; Kinnunen, K.; Tuononen, H. M.; Väisänen, A.; Rissanen, K.; Haukka, M. Porous 3D Printed Scavenger Filters for Selective Recovery of Precious Metals from Electronic Waste. *Adv. Sustain Syst* **2018**, *2* (10), 1800048.
(33) Xu, J.; Slykas, C.; Braegelman, A. S.; Alvarez, K. G.; Kasl, T.; Boudouris, B. W.; Webber, M. J.; Sharma, V.; Phillip, W. A. Heavy Metal Removal Using Structured Sorbents 3D Printed from Carbon Nanotube-Enriched Polymer Solutions. *Matter* **2022**, *5*, 3432.
(34) Al-Shimmery, A.; Mazinani, S.; Flynn, J.; Chew, J.; Mattia, D. 3D Printed Porous Contactors for Enhanced Oil Droplet Coalescence. *J. Membr. Sci.* **2019**, *590*, 117274.
(35) Samanta, J.; Tang, M.; Zhang, M.; Hughes, R. P.; Staples, R. J.; Ke, C. Tripodal Organic Cages with Unconventional CH···O Interactions for Perchlorate Remediation in Water. *J. Am. Chem. Soc.* **2023**, *145* (40), 21723−21728.
(36) Walker, D. A.; Hedrick, J. L.; Mirkin, C. A. Rapid, Large-Volume, Thermally Controlled 3D Printing Using a Mobile Liquid Interface. *Science* **2019**, *366* (6463), 360−364.
(37) Preinerstorfer, B.; Lindner, W.; Lämmerhofer, M. Polymethacrylate-Type Monoliths Functionalized with Chiral Amino Phosphonic Acid-Derived Strong Cation Exchange Moieties for Enantioselective Nonaqueous Capillary Electrochromatography and Investigation of the Chemical Composition of the Monolithic Polymer. *Electrophoresis* **2005**, *26* (10), 2005−2018.
(38) Hoang, T. K. A.; Hamaed, A.; Moula, G.; Aroca, R.; Trudeau, M.; Antonelli, D. M. Kubas-Type Hydrogen Storage in V(III) Polymers Using Tri- and Tetradentate Bridging Ligands. *J. Am. Chem. Soc.* **2011**, *133* (13), 4955−4964.
(39) Mehmood, T.; Iqbal, M. Optimized Extraction of Pb (II) and Co (II) with Glycolamide Mono and Di-Ionic Liquids Using Response Surface Methodology. *J. Chemom* **2021**, *35* (12), No. e3382.
(40) Dong, Z.; Cui, H.; Zhang, H.; Wang, F.; Zhan, X.; Mayer, F.; Nestler, B.; Wegener, M.; Levkin, P. A. 3D Printing of Inherently Nanoporous Polymers via Polymerization-Induced Phase Separation. *Nat. Commun.* **2021**, *12*, 247.
(41) Schneider, C. A.; Rasband, W. S.; Eliceiri, K. W. NIH Image to ImageJ: 25 Years of Image Analysis. *Nat. Methods* **2012**, *9* (7), 671−675.
(42) Sankur, B. Survey over Image Thresholding Techniques and Quantitative Performance Evaluation. *J. Electron Imaging* **2004**, *13* (1), 146.
(43) Bagheri, A.; Jin, J. Photopolymerization in 3D Printing. *ACS Applied Polymer Materials.* **2019**, *1*, 593−611.
(44) Ahn, D.; Stevens, L. M.; Zhou, K.; Page, Z. A. Additives for Ambient 3D Printing with Visible Light. *Adv. Mater.* **2021**, *33* (44), 2104906.
(45) Bae, Y.-S.; Yazaydın, A. O; Snurr, R. Q. Evaluation of the BET Method for Determining Surface Areas of MOFs and Zeolites That Contain Ultra-Micropores. *Langmuir* **2010**, *26* (8), 5475−5483.
(46) Bikas, H.; Stavropoulos, P.; Chryssolouris, G. Additive Manufacturing Methods and Modeling Approaches: A Critical Review. *International Journal of Advanced Manufacturing Technology* **2016**, *83* (1−4), 389−405.
(47) He, P.; Tang, X.; Chen, L.; Xie, P.; He, L.; Zhou, H.; Zhang, D.; Fan, T. Patterned Carbon Nitride-Based Hybrid Aerogel Membranes via 3D Printing for Broadband Solar Wastewater Remediation. *Adv. Funct Mater.* **2018**, *28* (29), 1801121.
(48) Sano, M.; Maruo, T.; Masuda, Y.; Yamatera, H. EXAFS Studies on the Methanol and Ethanol Solutions of Cobalt(II) Bromides. *J. Solution Chem.* **1986**, *15* (10), 803−809.
(49) Luz, Z. Nuclear Magnetic Resonance and Optical Spectroscopy of [Co(MeOH)5Cl]+ in Methanol and the Kinetics of Methanol Exchange of the Solvation Shell. *J. Chem. Phys.* **1964**, *41* (6), 1748−1755.
(50) Wertz, D. L.; Kruh, R. F. X-Ray Diffraction Study of Some Concentrated Cobalt(II) Chloride Solu-tions. *J. Chem. Phys.* **1969**, *50* (10), 4313−4317.
(51) Chiban, M.; Soudani, A.; Sinan, F.; Persin, M. Single, Binary and Multi-Component Adsorption of Some Anions and Heavy Metals on Environmentally Friendly Carpobrotus Edulis Plant. *Colloids Surf. B Biointerfaces* **2011**, *82* (2), 267−276.
(52) Yang, Y.; Yang, Y.; He, C.; Wei, Y.; Fujita, T.; Wang, G.; Ma, S.; Yang, W. Solvent Extraction and Separation of Cobalt from Leachate of Spent Lithium-Ion Battery Cathodes with N263 in Nitrite Media. *International Journal of Minerals, Metallurgy and Materials* **2023**, *30* (5), 897−907.
(53) Zhang, M.; Zhang, Y.; Helleur, R. Selective Adsorption of Ag+ by Ion-Imprinted O-Carboxymethyl Chitosan Beads Grafted with Thiourea-Glutaraldehyde. *Chemical Engineering Journal* **2015**, *264*, 56−65.
(54) Mack, C.; Wilhelmi, B.; Duncan, J. R.; Burgess, J. E. Biosorption of Precious Metals. *Biotechnol Adv.* **2007**, *25* (3), 264−271.
(55) Miessler, G.; Tarr, D. *Inorganic Chemistry*, 4th ed.; Prentice Hall, 2011; pp 395−396.
(56) Nitta, N.; Wu, F.; Lee, J. T.; Yushin, G. Li-Ion Battery Materials: Present and Future. *Mater. Today* **2015**, *18* (5), 252−264.

https://doi.org/10.1021/jacs.3c12635
J. Am. Chem. Soc. 2024, 146, 4078−4086